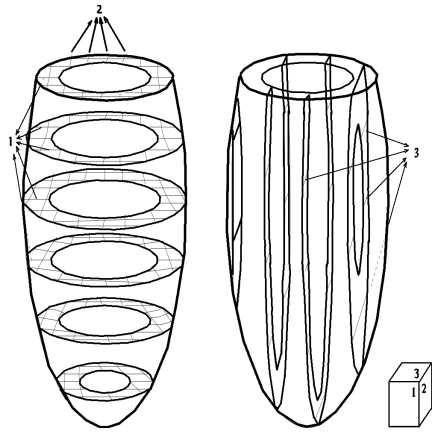


(a) Short-axis tag data (b) long-axis tag data

**Figure 1.** The cube in the lower right illustrates the three orthogonal directions of the tag plane normals. The intersection of the short-axis image planes with the short-axis tag planes results in the tag lines marked '1' and '2.' Similarly, the tag lines marked '3' are formed from the intersection of the long-axis image planes with the long-axis tag planes.

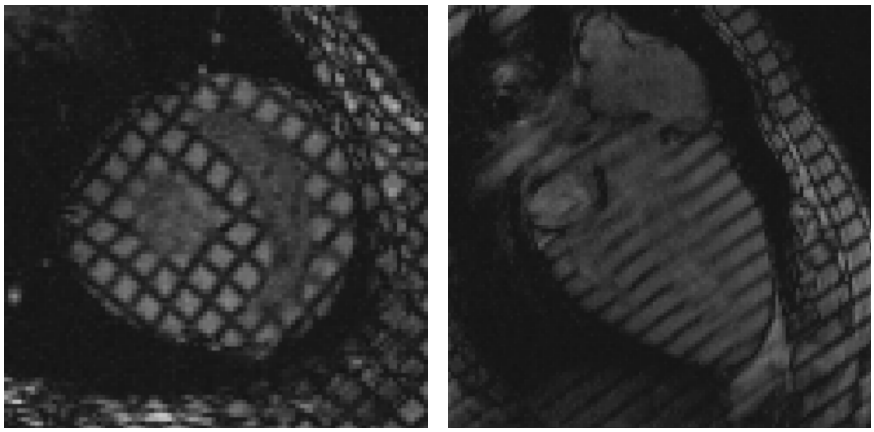

(a) (b)

**Figure 2.** MR images from a canine study showing the left and right ventricles in both (a) the short- and (b) long-axis views.

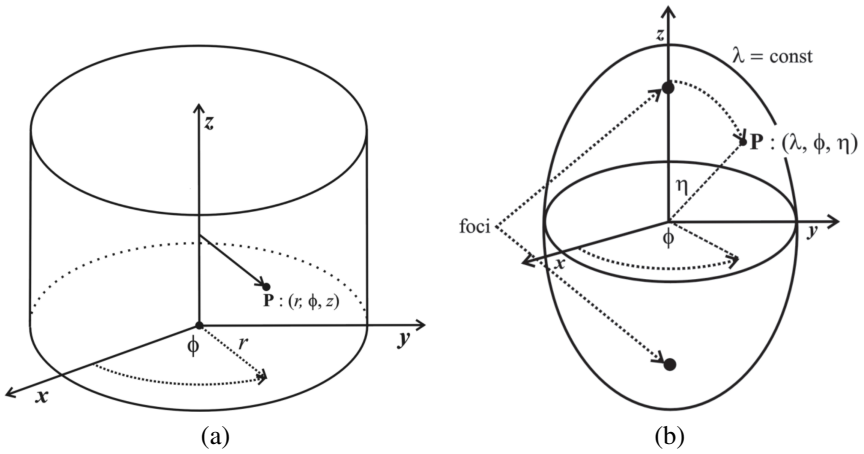


**Figure 3.** (a) Cylindrical coordinate system; (b) prolate spheroidal coordinate system used in constructing the NURBS model.

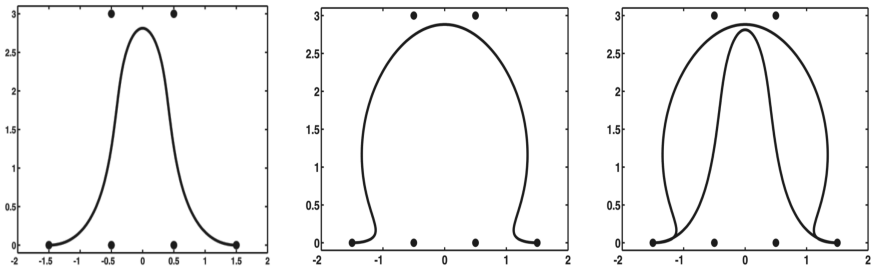


**Figure 4.** Cartesian versus non-Cartesian nonrational B-spline curves: order = 4; control point coordinates $(x, y)$ — $\mathbf{P}_1 = (-1.5, 0)$, $\mathbf{P}_2 = (-0.5, 0)$, $\mathbf{P}_3 = (-0.5, 3)$, $\mathbf{P}_4 = (0.5, 3)$, $\mathbf{P}_5 = (0.5, 0)$, $\mathbf{P}_6 = (1.5, 0)$. Illustrated are (a) the Cartesian B-spline curve, (b) the polar-based B-spline curve, and (c) their superposition constructed from the control points.

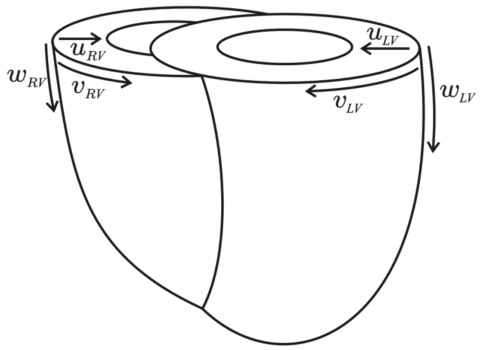


**Figure 5.** Parametric directions of the left- and right-ventricular NURBS model given by $(u_{LV}, v_{LV}, w_{LV})$ and $(u_{RV}, v_{RV}, w_{RV})$, respectively.

**Figure 6.** Initial NURBS model of a canine heart constructed from the left- and right-ventricular contours.

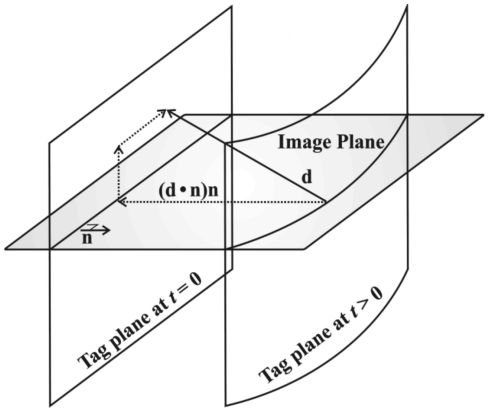


**Figure 7.** Diagrammatic representation of available measurements for model fitting. The only discernible measurement of the true displacement, $\mathbf{d}$, is the orthogonal component at time $t > 0$ to the tag plane configuration at time $t = 0$.

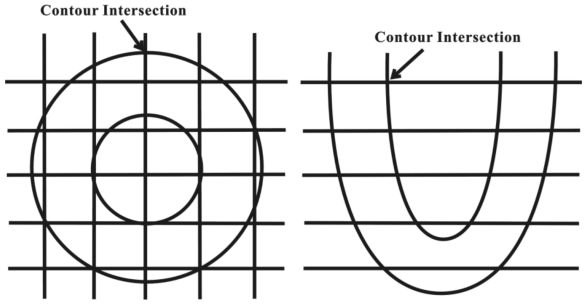


(a) Short-axis measurements (b) Long-axis measurements

**Figure 8.** Diagrammatic representation of additional measurements for model fitting consisting of the contour intersection points in the short- and long-axis views.

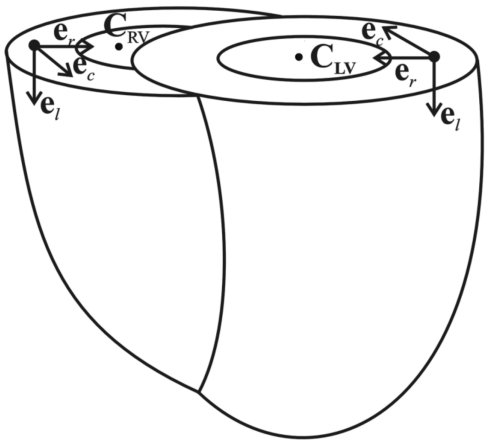


**Figure 9.** Strain calculation directions for both the left and right ventricles given by the orthonormal basis $\{\mathbf{e}_r, \mathbf{e}_c, \mathbf{e}_l\}$. The centers of the left and right ventricles are shown by the points $\mathbf{C}_{\mathrm{LV}}$ and $\mathbf{C}_{\mathrm{RV}}$, respectively.

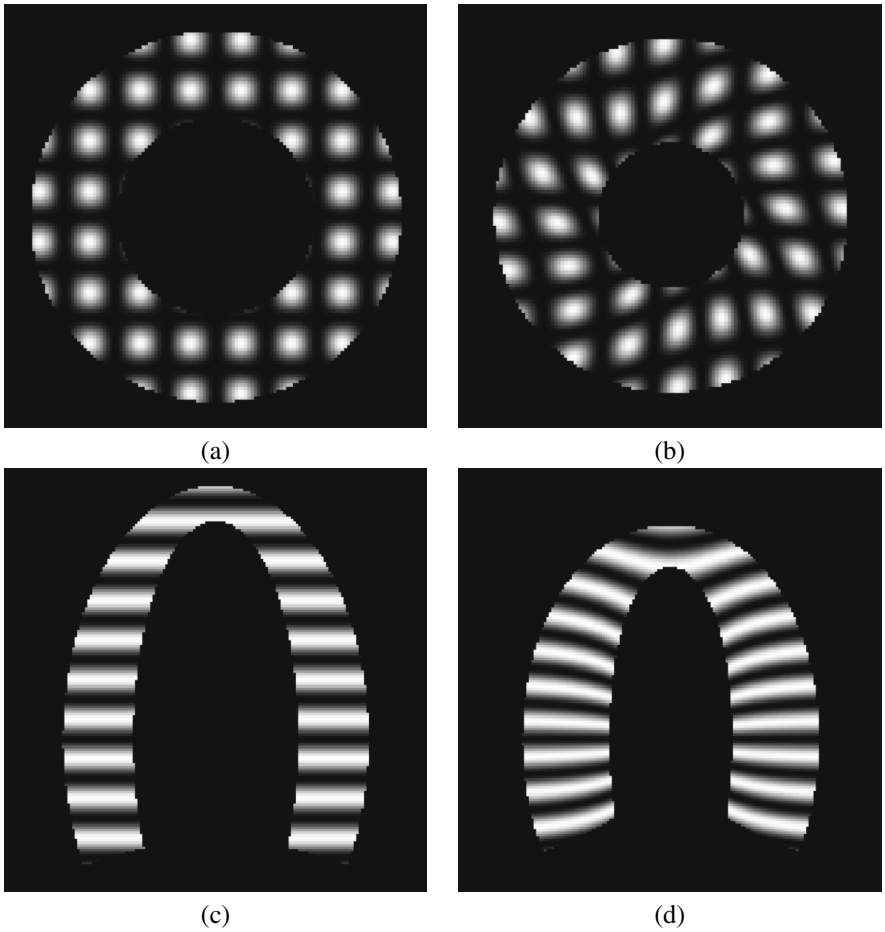


**Figure 10.** Simulated images generated from Arts' left-ventricular analytical model. A basal short-axis image is shown at (a) end-diastole and (b) end-systole. Similarly, long-axis images at (c) end-diastole and (d) end-systole are also illustrated.

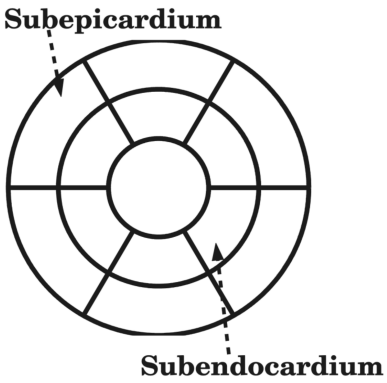


**Figure 11.** Diagrammatic representation of the regional division for analysis using Arts' model for a basal or mid-cavity short-axis view. The arrows point to one of six subendocardial or subepicardial regions.

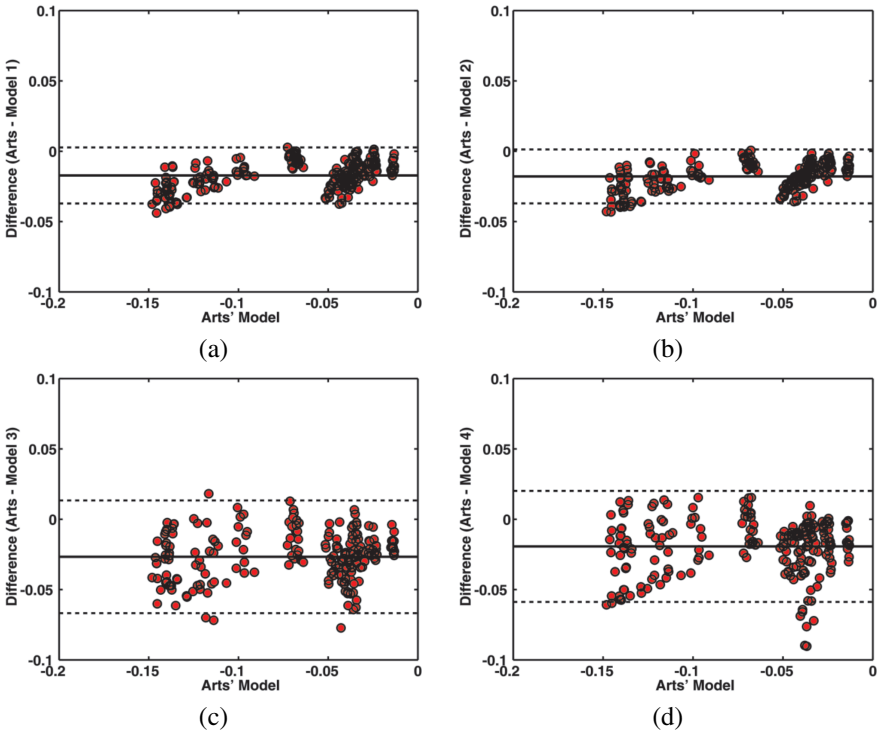


**Figure 12.** Bland-Altman plots for the best circumferential strain predictors of each model type. Plotted are the difference between Arts' model and the best performer from each model type of the 224 total models. Also included are the mean of the difference (solid line) and the 95% limits of agreement (dashed lines). (a) Cartesian-based cylindrical-parameterized NURBS model (order = 3, number of control points in $(u_{LV}, v_{LV}, w_{LV}) = (3, 4, 4)$). (b) Cartesian-based prolate spheroidal-parameterized NURBS model (order = 3, number of control points in $(u_{LV}, v_{LV}, w_{LV}) = (3, 4, 4)$). (c) Cylindrical-based cylindrical-parameterized NURBS model (order = 3, number of control points in $(u_{LV}, v_{LV}, w_{LV}) = (3, 3, 3)$). (d) Prolate spheroidal-based prolate spheroidal-parameterized NURBS model (order = 3, number of control points in $(u_{LV}, v_{LV}, w_{LV}) = (3, 5, 5)$).

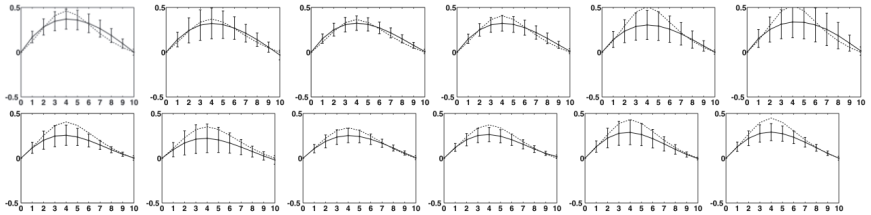

**Figure 13.** Average subendocardial radial strain plots across 112 NURBS model variants showing the mean (solid line) and standard deviation (error bars) for the predicted strain values for the six basal (top row) and six mid-cavity (bottom row) regions. The dashed line represents the ground truth strain value predicted by the analytical model.

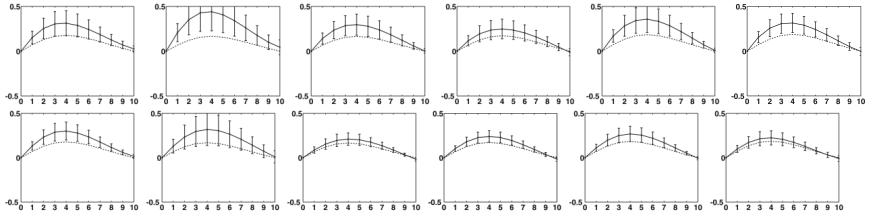

**Figure 14.** Average subepicardial radial strain plots across 112 NURBS model variants showing the mean (solid line) and standard deiation (error bars) for the predicted strain values for the six basal (top row) and six mid-cavity (bottom row) regions. The dashed line represents the ground truth strain value predicted by the analytical model.

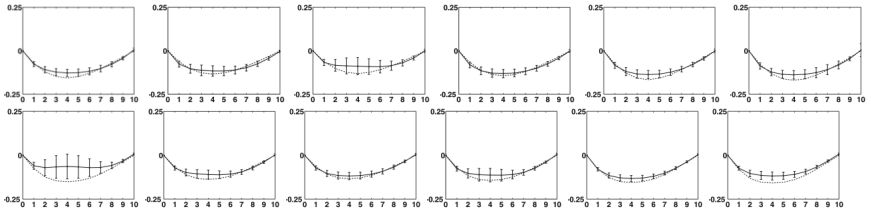

**Figure 15.** Average subendocardial circumferential strain plots across 112 NURBS model variants showing the mean (solid line) and standard deviation (error bars) for the predicted strain values for the six basal (top row) and six mid-cavity (bottom row) regions. The dashed line represents the ground truth strain value predicted by the analytical model.

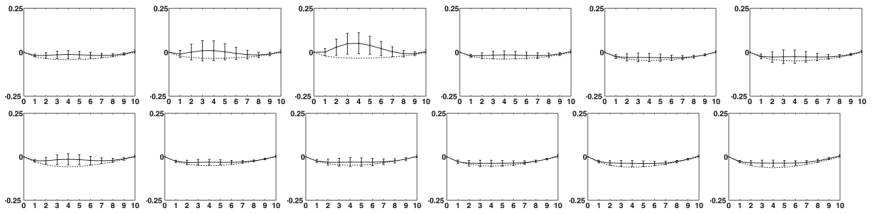

**Figure 16.** Average subepicardial circumferential strain plots across 112 NURBS model variants showing the mean (solid line) and standard deviation (error bars) for the predicted strain values for the six basal (top row) and six mid-cavity (bottom row) regions. The dashed line represents the ground truth strain value predicted by the analytical model.

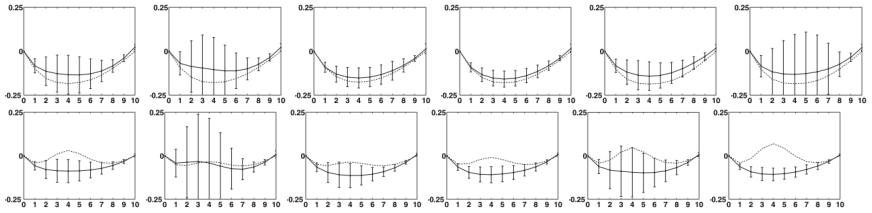

**Figure 17.** Average subendocardial longitudinal strain plots across 112 NURBS model variants showing the mean (solid line) and standard deviation (error bars) for the predicted strain values for the six basal (top row) and six mid-cavity (bottom row) regions. The dashed line represents the ground truth strain value predicted by the analytical model.

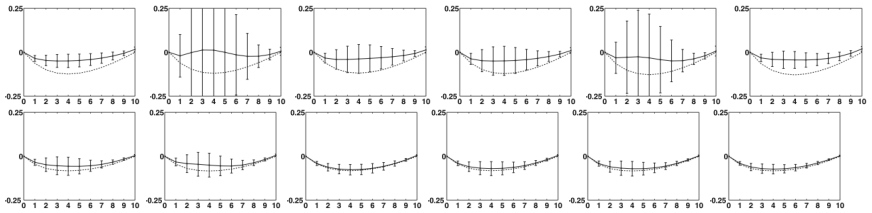

**Figure 18.** Average subepicardial longitudinal strain plots across 112 NURBS model variants showing the mean (solid line) and standard deviation (error bars) for the predicted strain values for the six basal (top row) and six mid-cavity (bottom row) regions. The dashed line represents the ground truth strain value predicted by the analytical model.

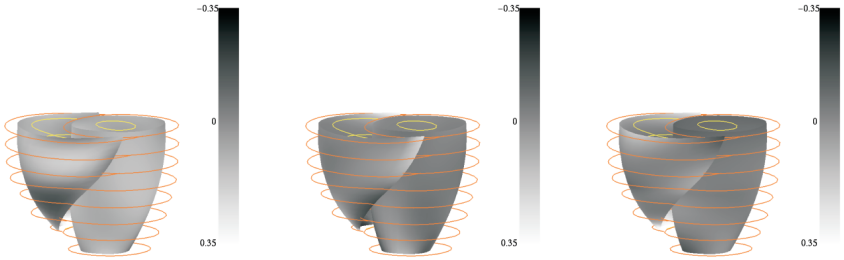


**Figure 19.** Qualitative peak strain results for a midventricular surface for the left ventricle ($u_{LV} = 0.5$) and right ventricle ($u_{RV} = 0.5$) of one dog study (Dog 3). Illustrated strains include (a) the radial strain, (b) the circumferential strain, and (c) the longitudinal strain.

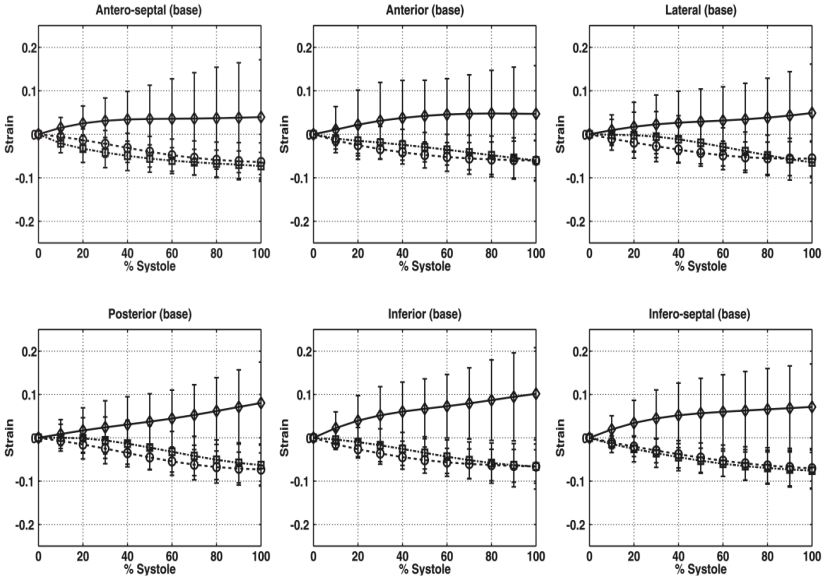


**Figure 20.** Average Lagrangian normal strain plots across three normal canine datasets for the six basal regions of the left ventricle. The different geometric shapes (diamond, circle, and square) represent the radial, circumferential, and longitudinal strain values, respectively. The $x$ axis marks the time point during systole.

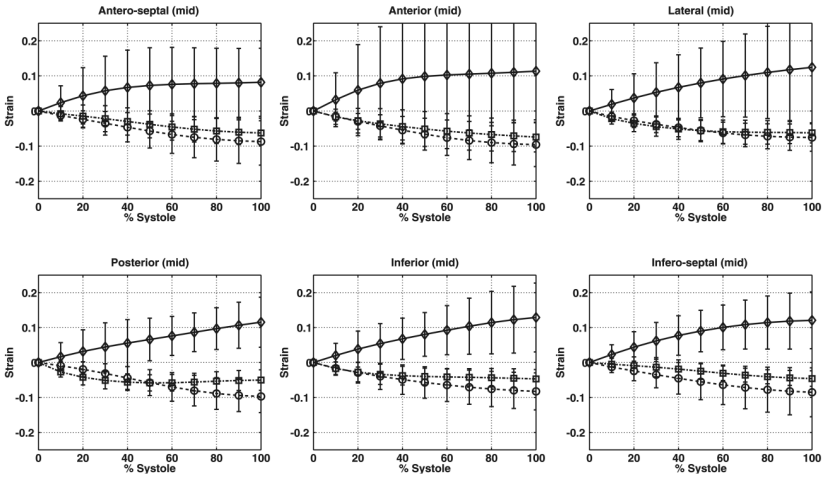


**Figure 21.** Average Lagrangian normal strain plots across three normal canine datasets for the six mid-cavity regions of the left ventricle. The different geometric shapes (diamond, circle, and square) represent the radial, circumferential, and longitudinal strain values, respectively. The $x$ axis marks the time point during systole.

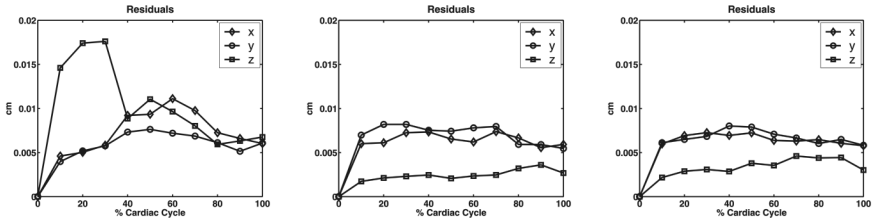


(a) (b) (c)

**Figure 22.** Average residuals per sample point for all three coordinates for $\mathcal{R}_t \rightarrow \mathcal{R}$ model registration for (a) Dog 1, (b) Dog 2, and (c) Dog 3. The $y$ axis has dimension of centimeters.

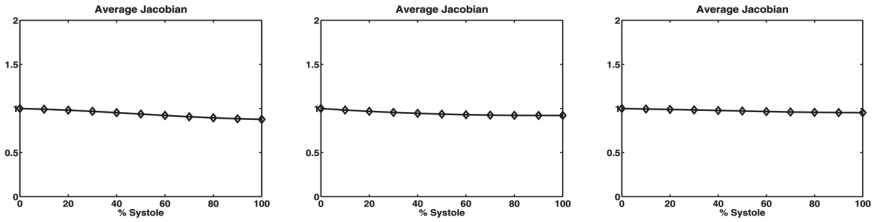


(a) (b) (c)

**Figure 23.** Average Jacobian (Lagrangian) over the twelve left-ventricular regions for (a) Dog 1, (b) Dog 2, and (c) Dog 3.

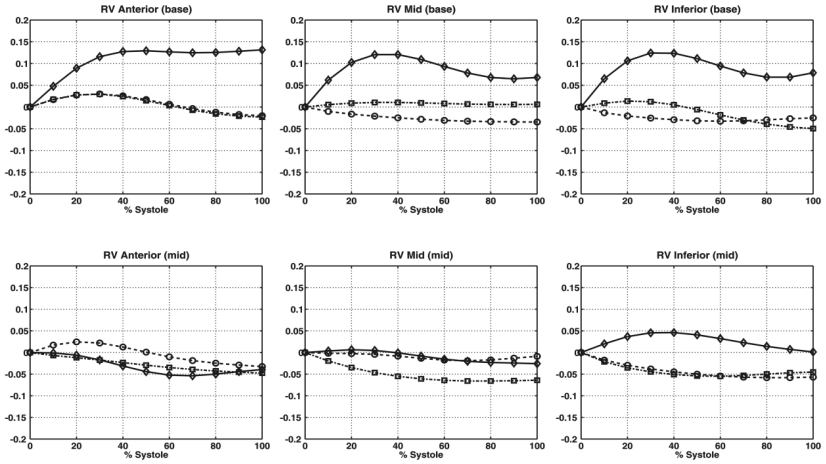


**Figure 24.** Average Lagrangian normal strain plots for one dog study (Dog 3) for the six basal and mid-cavity regions of the right ventricle. The different geometric shapes (diamond, circle, and square) represent the radial, circumferential, and longitudinal strain values, respectively. The $x$ axis marks the time point during systole.

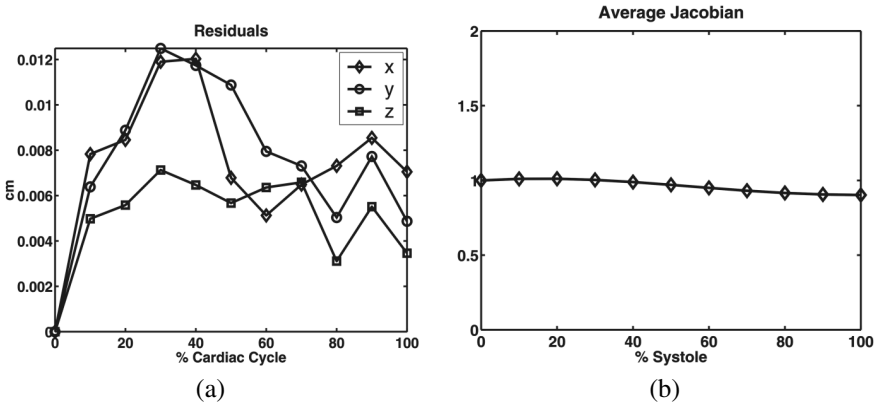


**Figure 25.** Assessment of a NURBS right-ventricular model for Dog 3 showing both (a) the average residual per sample point for all three coordinates for $\mathcal{R}_t \rightarrow \mathcal{R}$ model fitting and (b) the average Jacobian over systole.

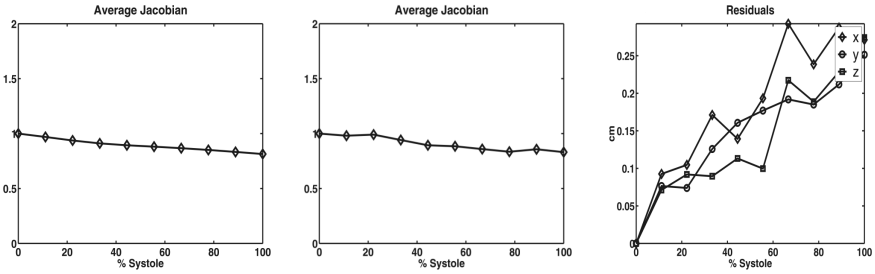


(a) (b) (c)

**Figure 26.** Metrics for the left ventricle of a normal human volunteer illustrated by (a) the Jacobian for the Lagrangian fit, (b) the Jacobian for the Eulerian fit that registers $\mathcal{R}_t \rightarrow \mathcal{R}$, and (c) the residuals for fitting $\mathcal{R}_t \rightarrow \mathcal{R}$.

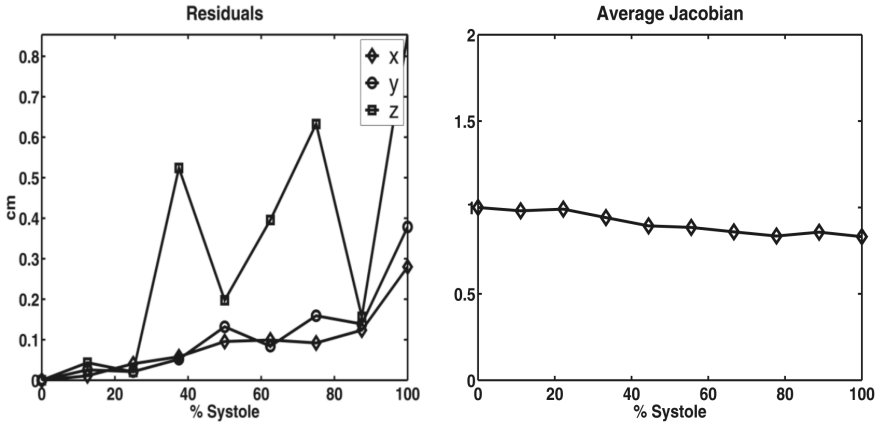


(a) (b)

**Figure 27.** Metrics for the left ventricle of a patient with a history of myocardial infarction illustrated by (a) the Jacobian for the Lagrangian fit that registers $\mathcal{R} \rightarrow \mathcal{R}_t$, and (b) the residuals for fitting$\mathcal{R}_t \rightarrow \mathcal{R}$.

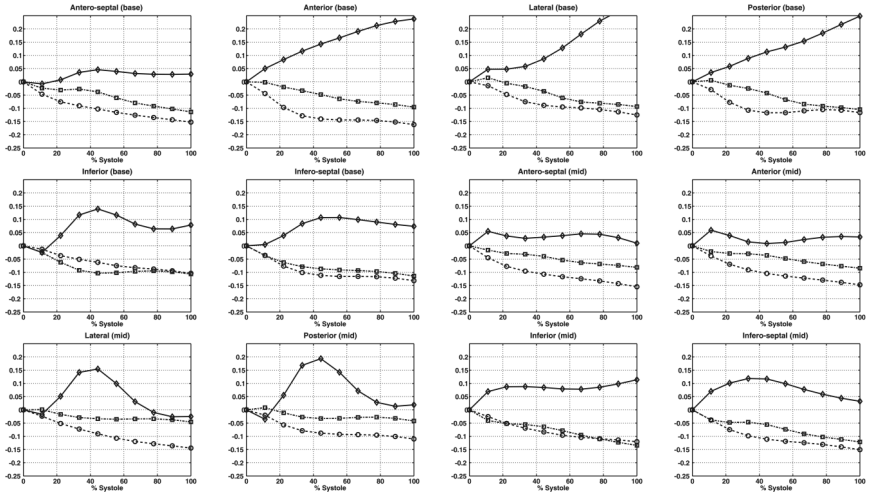


**Figure 28.** Average Lagrangian normal strain plots for the twelve basal and mid-cavity regions of the left ventricle of a normal human volunteer. The different geometric shapes (diamond, circle, and square) represent the radial, circumferential, and longitudinal strain values, respectively. The $x$ axis marks the time point during systole.

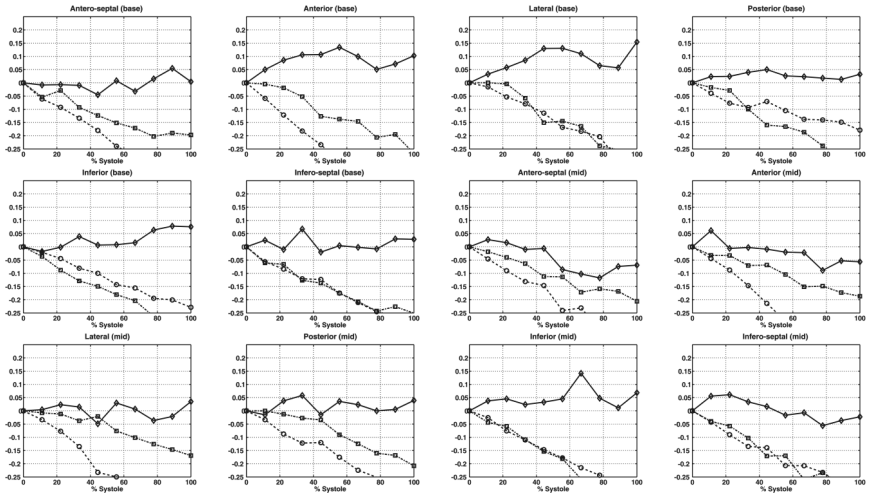


**Figure 29.** Average Eulerian normal strain plots for the twelve basal and mid-cavity regions of the left ventricle of a normal human volunteer. The different geometric shapes (diamond, circle, and square) represent the radial, circumferential, and longitudinal strain values, respectively. The $x$ axis marks the time point during systole.

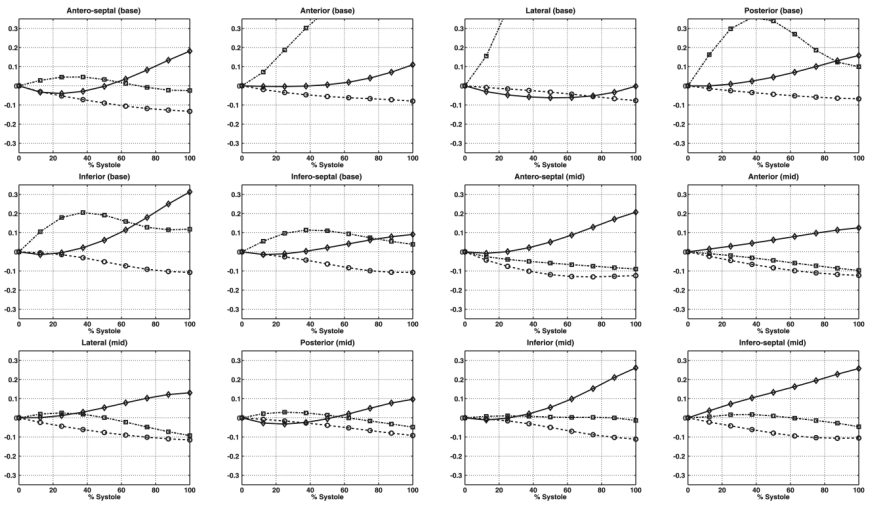


**Figure 30.** Average Lagrangian normal strain plots for the twelve basal and mid-cavity regions of the left ventricle of a patient with a history of myocardial infarction. The different geometric shapes (diamond, circle, and square) represent the radial, circumferential, and longitudinal strain values, respectively. The $x$ axis marks the time point during systole.